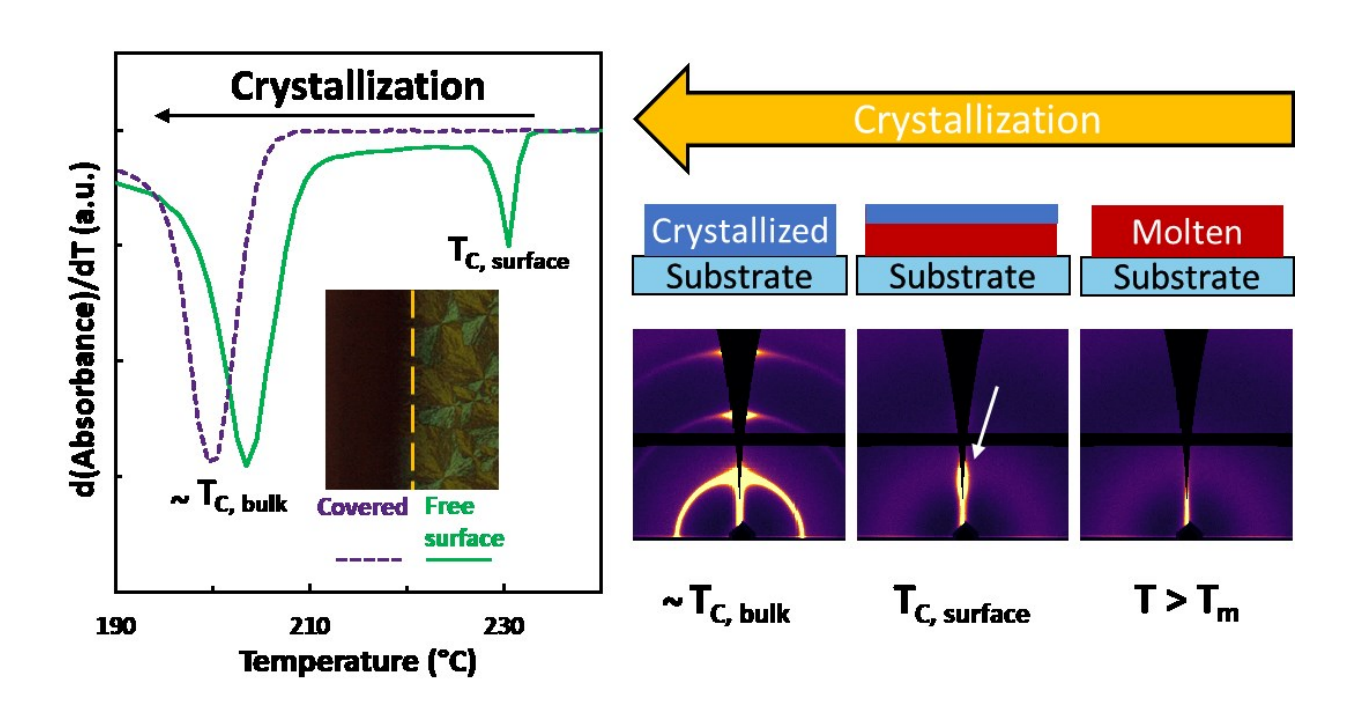
Direct observation of two-step, stratified crystallization and morphology in conjugated polymer thin films

Jesse Kuebler¹, Tucker Loosbrock¹, Joseph Strzalka², Lucia Fernandez-Ballester^{1*}

¹Department of Mechanical and Materials Engineering and Nebraska Center for Materials and Nanoscience, University of Nebraska at Lincoln, Lincoln, Nebraska 68588, United States.

²X-Ray Science Division, Argonne National Laboratory, Lemont, IL 60439, United States

For Table of Contents use only:



Keywords: conjugated polymers, crystallization, thin films, interfacial effects, free surface, orientation.

^{*}Corresponding author: Email: lucia.fernandez@unl.edu

Abstract

A two-step stratified crystallization process has been directly observed during cooling of poly(3-hexylthiophene) (P3HT) thin films of thickness h = 20-250 nm: a thin (<20 nm) layer at the free surface crystallizes ~25 °C higher than the bulk crystallization temperature ($T_{C,bulk}$), whereas the rest of the film (i.e. the underlayer) crystallizes near $T_{C,bulk}$. In-situ measurements of films with and without a free surface unequivocally ascribe the high-temperature crystallization to a surface-induced process, which correlates with formation of large birefringent structures and highly oriented edge-on crystallites at the air-polymer interface. In contrast, crystallization of the bulk-like underlayer leads to mostly edge-on oriented crystallites in thinner films and becomes increasingly isotropic in thicker films. For h < 20 nm, free-surface effects dominate and only the high temperature crystallization is observed. These results highlight the potential of melt-crystallization to tailor morphology and orientation across thin film thickness for specific electronic applications.

1 Introduction

Conjugated polymers are materials capable of charge transport with potential for application in light emitting diodes, photovoltaic devices, sensors, and other electronic devices. ¹⁻³ In semicrystalline conjugated polymers—for which poly(3-hexylthiophene) (P3HT) is considered a model—a strong relationship between processing, final semicrystalline structure, and conductive properties has been established but is still not fully understood. ⁴⁻¹² For electronic applications, thin films of conjugated polymers are typically solvent-processed due to ease of use and fast

processing times, but crystallization from solvents often yields semicrystalline structures very far from equilibrium which are susceptible to change above the glass transition temperature. In addition, polymer crystallization during solvent-processes such as spin coating or drop casting typically occurs under ill-defined conditions, hindering the ability to control the final semicrystalline morphology. In contrast, melt-processing of films—in the absence of solvents—can enable greater control over the conditions under which crystallization occurs.

The potential of melt-crystallization to attain optimized morphologies in conjugated polymer thin films remains largely untapped, partly because it has been much less studied than solution crystallization during solvent-based processing. 14-22 Furthermore, the melt-crystallization behavior of thin films cannot be inferred from bulk measurements due to the possibility of confinement effects as well as interfacial effects near the substrate and the air-polymer boundary. 23 As a result, there is a critical need to understand the melt-crystallization process throughout the conjugated film thickness, especially given that device performance can be dictated by the semicrystalline structure at different depths of the film. 19, 24-28 For example, performance of field effect transistors is dominated by the few nm closest to an active film interface, whereas applications such as photovoltaics depend on structure and charge transport across the entire film thickness. 29-34

The role that the polymer-air interface plays in melt-crystallization of conjugated thin films is currently poorly understood. While free surfaces are generally known to influence properties such as glass transition and melting temperatures, the specific effects are not universal across materials. For example, most small molecules exhibit surface melting, i.e. reduced melting temperature at the free surface attributed to higher surface entropy.³⁵ Similarly, polymers such

as PS, PET, and PMMA exhibit reduced surface glass transition (T_g) and cold crystallization temperatures due to increased chain mobility at the surface. ³⁶⁻³⁸ In contrast, linear alkanes and the alkyl side chains of polyacrylates exhibit surface freezing, i.e. increased surface solidification temperatures. Surface freezing is attributed to a lower interfacial energy, γ , in the surface frozen state ($\gamma_{cry,air} + \gamma_{cry,liq}$) compared to the fully molten state ($\gamma_{liq,air}$) which drives the transition. Preferential orienting of molecules at the free surface frequently accompanies surface freezing and is thought to arise when a given orientation is energetically more favorable, minimizing $\gamma_{cry,air} + \gamma_{cry,liq}$. ^{35, 39-44} Some alkyl-chain polymers—namely APFO₃ and PFO—have exhibited increased surface glass transition, cold-crystallization, and melting temperature during heating. ⁴⁵ Surface freezing has been proposed to explain ex-situ preferential orientation near the surface of P3HT films, but has not been directly observed in-situ. ⁴³⁻⁴⁴ Overall, the role of the air-polymer interface on the melt-crystallization process at various film depths remains elusive.

To address this gap in knowledge, it is critical to apply experimental in-situ approaches that can isolate the effect of an interface, which entails significant technical challenges. On one hand, experimental techniques must be extremely sensitive to crystallization, given that the film interface contains a minute amount of crystallizing material. Even greater sensitivity is required for in-situ measurements, where structure development occurs rapidly and acquisition times must be small. On the other hand, experimental techniques that can isolate free surface effects often have drawbacks that complicate their application to thin film melt-crystallization. For example, incorporating fluorescent markers only at a specific film depth has enabled the measurement of depth-dependent $T_{\rm g}$, 36 but is unsuitable for melt-crystallization as the markers would quickly diffuse to other depths of the film at the high temperatures involved. Techniques

such as variable temperature spectroscopic ellipsometry require models and significant a priori knowledge about the material phases involved to extract depth-dependent information,⁴⁵ while surface sensitive techniques such as grazing incidence wide angle X-ray scattering (GIWAXS) and atomic force microscopy require a free surface, preventing direct comparison between films with and without an air-polymer interface.

In this work, we use a combination of in-situ UV-vis optical absorbance and reflectance, microscopy, and variable-angle GIWAXS to study free surface-induced morphological and orientation effects during melt-crystallization of P3HT thin films. By applying in-situ optical techniques that are extremely sensitive to crystallization and do not require a free surface, we are able to directly compare films with and without an air-polymer interface to isolate the free-surface effects on the melt-crystallization process. Furthermore, in-situ optical absorption measurements allow estimating the small layer thickness at the air-polymer interface that is dominated by free surface-induced crystallization. In-situ angle-dependent GIWAXS allows establishing the connection between crystallization events that occur at different depths/temperatures and corresponding morphological characteristics—such as crystalline orientation—relevant to applications.

2 Experimental

2.1 Materials

Poly(3-hexylthiophene) (P3HT, 95% regioregular, weight-averaged molecular weight M_W = 40 kg/mol, polydispersity index PDI = 2.1) from Rieke Metals was used as received.

2.2 Film preparation

P3HT solutions in o-dichlorobenzene (Sigma Aldrich) were prepared by stirring at 80 °C for ~24 h under argon atmosphere with polymer concentration between 2 and 30 mg/mL. Prior to spin coating or drop casting, the solutions were heated to 100 °C for 10 min. Thin films were spin coated (SC) on cleaned glass coverslips or silicon wafers with 285 nm thermal oxide layer (University Wafer). SC films for optical microscopy (OPM) were cut into smaller pieces, floated on deionized water, transferred to new plasma cleaned glass coverslips, and dried at 100 °C for 20 min. To remove the free surface, a SC film was heated to 280 °C in argon atmosphere and a small piece of glass was pressed onto the molten film. SC films for Grazing incidence wide-angle X-ray scattering (GIWAXS) measurements were prepared on silicon wafers 18 mm x 18 mm. Film thicknesses were measured with profilometry using a Keyence VK-X200K laser scanning microscope. A thick film (~3 μm) for OPM was drop casted by depositing 20 μL of 30 mg/mL solution onto a cleaned coverslip and heating at 150 °C until dry. A second, cleaned coverslip was then placed over half the film, and the sample was melted to the coverslip under argon atmosphere.

2.3 Characterization

Optical micrographs were taken with an Olympus BX53M polarizing optical microscope equipped with a SC50 camera. UV-vis spectra were simultaneously collected using a beam splitter and fiber optic cable coupled to an Ocean Insight Flame-S spectrophotometer. Polarized reflection micrographs and reflectance spectra were acquired using a polarizer and analyzer crossed at 90°, whereas transmission micrographs and absorbance spectra were acquired with no polarizer or analyzer. Thermal cycles were performed with a Linkam THMS600 stage using 10

 $^{\circ}$ C/min heating and cooling rates. Samples were held at 270 $^{\circ}$ C for 5 min prior to cooling. There is no significant vertical thermal gradient in the film due to the experimental setup (<1 $^{\circ}$ C for $^{\sim}$ 250 nm films, Figure S1 in Supplemental Data). Light exposure was minimized using a homemade shutter. Absorbance spectra were calculated as the natural log of the ratio between the incident (reference) and transmitted intensity. Reflectance spectra were calculated as the ratio between the reflected and reference intensity (acquired using a mirror). The absorbance and reflectance spectra were averaged between 570 and 640 nm (Figure 1), then the numerical derivative with respect to temperature was calculated to assess the relative change with temperature. The 570-640 nm absorbance range encompasses the A₀₋₀ vibronic peak attributed to weakly interacting H-aggregates along the π - π stacking direction, $^{47-48}$ but random coiled chains in the molten state (Figure 1, 234 $^{\circ}$ C) do not significantly contribute to 570-640 nm absorbance. Therefore, the average signal from 570-640 nm allows tracking of π - π aggregation during crystallization without contribution from molten amorphous polymer.

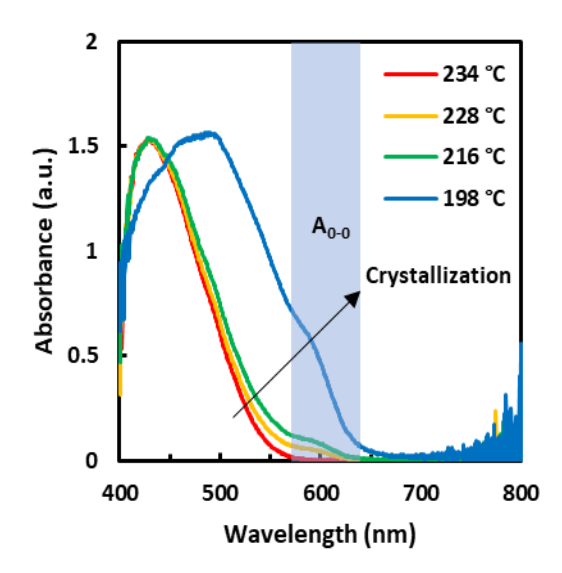


Figure 1: Absorbance spectra during crystallization of a 250 nm thick film. Arrow indicates decreasing temperature. Blue shaded area indicates the 570-640 nm range.

Bulk crystallization behavior was characterized using differential scanning calorimetry (DSC) on a TA Instruments DSC250 Discovery Series under nitrogen atmosphere and heating/cooling rates of 10 °C/min. To mimic conditions of solution processed thin films, a ~3 mg DSC bulk sample was also prepared from a 30 mg/mL solution by drop casting into a pan and drying under vacuum at 120 °C for 48 hrs.

GIWAXS patterns were collected at the 8-ID-E beamline (Advanced Photon Source, Argonne National Laboratory)⁴⁹ using incident X-rays with energy 10.92 keV, defined by slits to size 200 μ m x 10 μ m (H x V), at angles of incidence α_i = 0.08° and 0.14° for surface and bulk measurements, respectively. 2D diffraction patterns were collected with a Pilatus 1M detector (0.172 mm x 0.172 mm pixel size) positioned 217 mm from the sample. Alignment of samples was performed at 210 °C (near the temperatures at which crystallization events occur). The 2D patterns were corrected

for geometry and remapped using the GIXSGUI MATLAB package.⁵⁰ GIWAXS patterns were azimuthally integrated across wedges of width $\Delta \chi = 1^{\circ}$ (Figure S2a in Supplemental Data) to calculate the intensity vs. q at each azimuthal angle χ (Figure S2b). The contributions from the background, amorphous, and (100) scattering were simultaneously fitted using an exponential for the background, a Gaussian for the amorphous contribution, and a Gaussian for the (100) peak (Figure S2b). Coherence lengths were estimated using the Scherrer equation and the radial (along q) full width at half max (FWHM) after correcting for instrument broadening. 51 The (010) paracrystallinity was calculated according to the single-peak method which has been validated for high M_W thiophene-based polymers in the π - π stacking direction.^{8, 52} The integrated (100) intensity at each χ were plotted into a pole figure (Figure S2c). Note that under grazing incidence geometry, no data can be acquired for χ less than the Bragg angle ($\theta_{(100)} \sim 1.93^{\circ}$). The minimum (100) intensity in the pole figure corresponds to isotropic scattering (shaded area in Figure S2c). A geometrical sine correction was applied to generate corrected pole figures where the intensity is proportional to the amount of crystallites oriented at each χ.⁵³⁻⁵⁴ Crystallization derivatives of the sine corrected (100) intensity at azimuthal angles $\chi = 2.5^{\circ}$, 10.5°, and the isotropic baseline were calculated using $\chi = 2-3^{\circ}$, 10-11°, and 70-75° wedges respectively. Scattering due to edgeon crystallites was estimated by subtracting the isotropic contribution, and the azimuthal FWHM of the edge-on scattering fraction was estimated to characterize the degree of orientation of edge-on crystallites (Figure S3).

3 Results

3.1 Distinct crystallization morphology on the free surface

Upon melt-crystallization of a ~3 μ m thick P3HT film which is partially covered with a glass coverslip, distinct spherulitic structures exhibiting a Maltese cross are observed only when a free surface is available, whereas no large-scale birefringent morphologies can be discerned in areas covered with the coverslip (Figure 2a). The spherulitic structures can be clearly observed when imaged in polarized reflection mode from the free surface side but cannot be detected from the bottom substrate side (Figure 2b). Given that the diameter of the spherulitic structures is much larger than the film thickness (~30-50 μ m vs. ~3 μ m), it is inferred that they only form near the top free surface and do not span the entire thickness of the film: light entering the film from the substrate side is absorbed before reaching and reflecting back from the spherulitic structures (note that light transmission through a ~3 μ m film is minimal, Figure 2c). In other words, the spherulitic structures appear to not grow into spherical objects but are instead discs confined within a thin layer near the free surface of the polymer film.

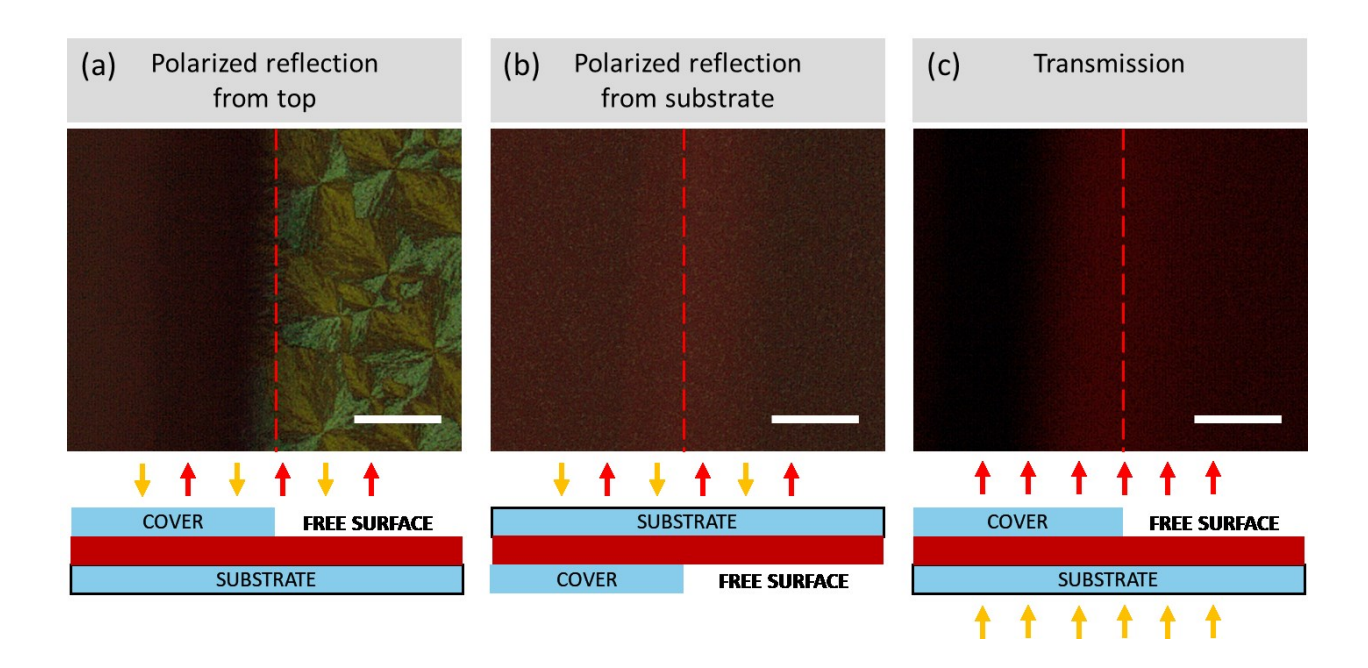


Figure 2: Micrographs of melt-crystallized ~3 μ m thick P3HT film partially covered by glass in (a) polarized reflection from top, (b) polarized reflection from substrate, and (c) transmission. Scalebar represents 50 μ m.

In much thinner spin coated films that allow significant light transmission (Figure 3c and f), the spherulitic structures are visible in polarized reflection both from the free surface and the substrate side, but their appearance is color shifted and more subdued when imaging the 250 nm film from the substrate side compared to imaging from the free surface (Figure 3a vs. b), and compared to imaging the 40 nm film from the substrate side (Figure 3b vs. e). This suggests that, even for a 250 nm film, the free surface spherulitic layer does not span the entire thickness of the film: light entering from the substrate side undergoes absorption by a non-spherulitic P3HT layer and results in an apparent color shift of the free surface structures.

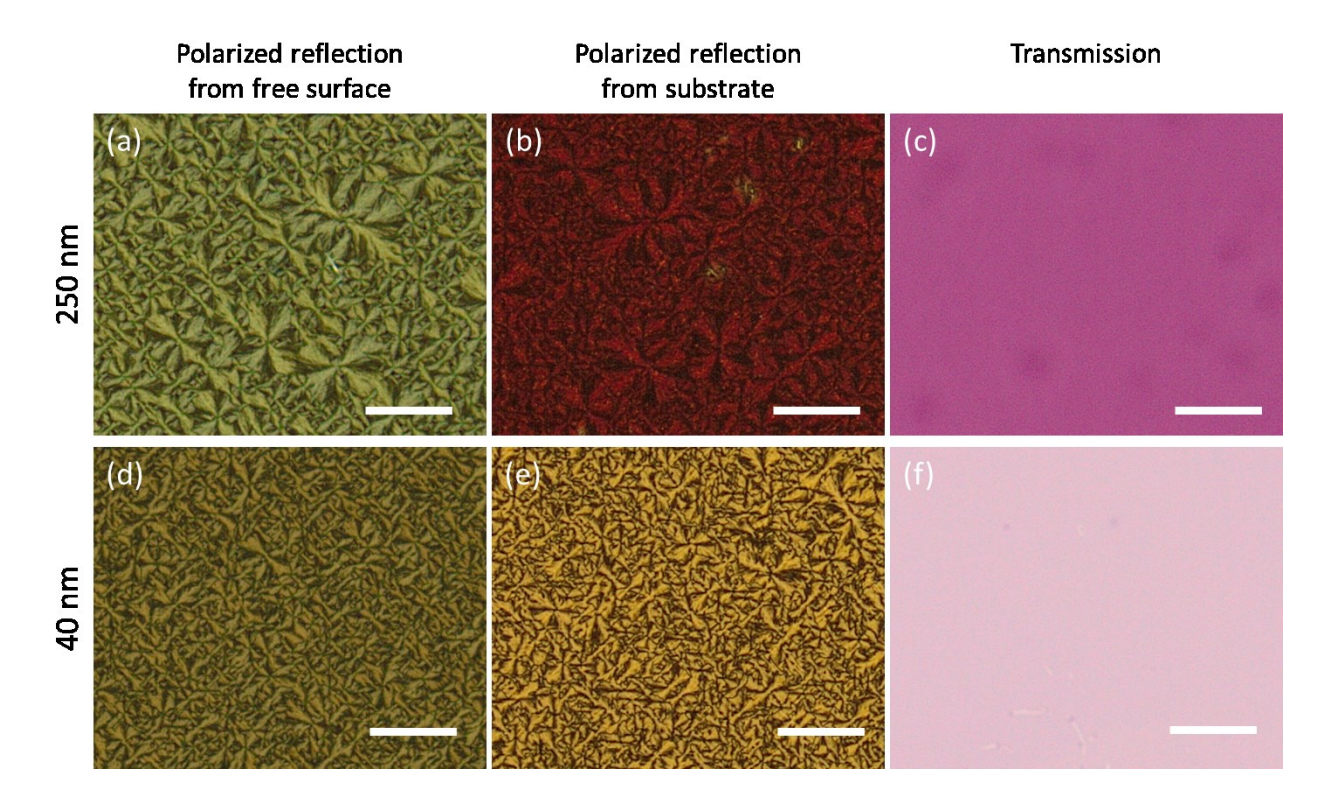


Figure 3: Micrographs of melt-crystallized P3HT films with thickness of (a-c) 250 nm and (d-f) 40 nm. (a,d) Polarized reflection from the free surface, (b,e) polarized reflection from the substrate side, and (c,f) transmission. Scalebar represents 50 μ m.

3.2 2-step stratified crystallization

The P3HT crystallization process was probed using in-situ absorbance measurements in the 570-640 nm wavelength range, where absorbance strongly depends on π - π aggregation and is negligible for molten, random P3HT coils (Figure 1). Because absorbance and optical microscopy do not require a free surface, films with a free surface and films covered with a top glass coverslip were both probed in-situ, and their direct comparison allowed isolating the effect of the free surface on the process of melt-crystallization.

For a 250 nm thick film where a free surface is present, the absorbance derivative exhibits two main crystallization events significantly separated in temperature by ~25 °C, whereas a 250 nm covered film only exhibits a single crystallization process (Figure 4a). Clearly, the absorbance crystallization curve for the free surface film exhibits a high temperature crystallization peak (T_{C1}) at ~230 °C and a low temperature crystallization peak (T_{C2}) at ~203 °C, while the high temperature crystallization peak is absent for the covered film lacking a free surface. Therefore, the high temperature T_{C1} peak corresponds to a free surface-induced crystallization process.

In-situ polarized reflection micrographs (Figure 4d) clearly show that the T_{C1} peak corresponds to lateral growth and impingement of spherulitic structures at the free surface. Indeed, when the film is covered with glass and the T_{C1} peak is no longer present, spherulitic structures are not apparent indicating that the free surface is required for their development. Likewise, in-situ polarized reflectance derivatives provide a qualitative measure of the emergence of birefringent structures and exhibit a large positive T_{C1} peak only for the free surface film (Figure 4c) that correlates with growth of spherulitic morphologies. It should be noted that spherulitic structures are obvious in polarized reflection imaging but cannot be distinguished by eye in transmission micrographs (Figure 4b)—even though absorbance measurements clearly detect the small change in intensity during T_{C1} crystallization.

The T_{C2} peak temperature of ~200 °C observed in both the free surface and the covered film approaches the P3HT bulk crystallization temperature ($T_{C,bulk}$ ~201.9 °C) measured by differential scanning calorimetry (Figure S6 in Supplemental Data), suggesting that a bulk-like crystallization process occurs at T_{C2} . Because the covered polymer film exhibits only T_{C2} crystallization, it is inferred that bulk-like crystallization occurs throughout the covered film thickness. The free

surface film, however, has already developed spherulitic structures at the top layer at T_{C1} , so the T_{C2} peak is inferred to arise from bulk-like crystallization of the rest of the film (i.e. the "underlayer" beneath the top, surface-induced spherulitic layer). Both the covered and the free surface film exhibit clear darkening in transmission micrographs and strong increase in absorbance at T_{C2} , indicating the growth of strongly absorbing crystallites (Figure 4a, b). At the same time, polarized reflection micrographs do not show any large birefringent structures at T_{C2} , and the negative peak in polarized reflectance derivative indicates that T_{C2} bulk-like crystallites do not significantly contribute to birefringence and that absorption effects dominate.

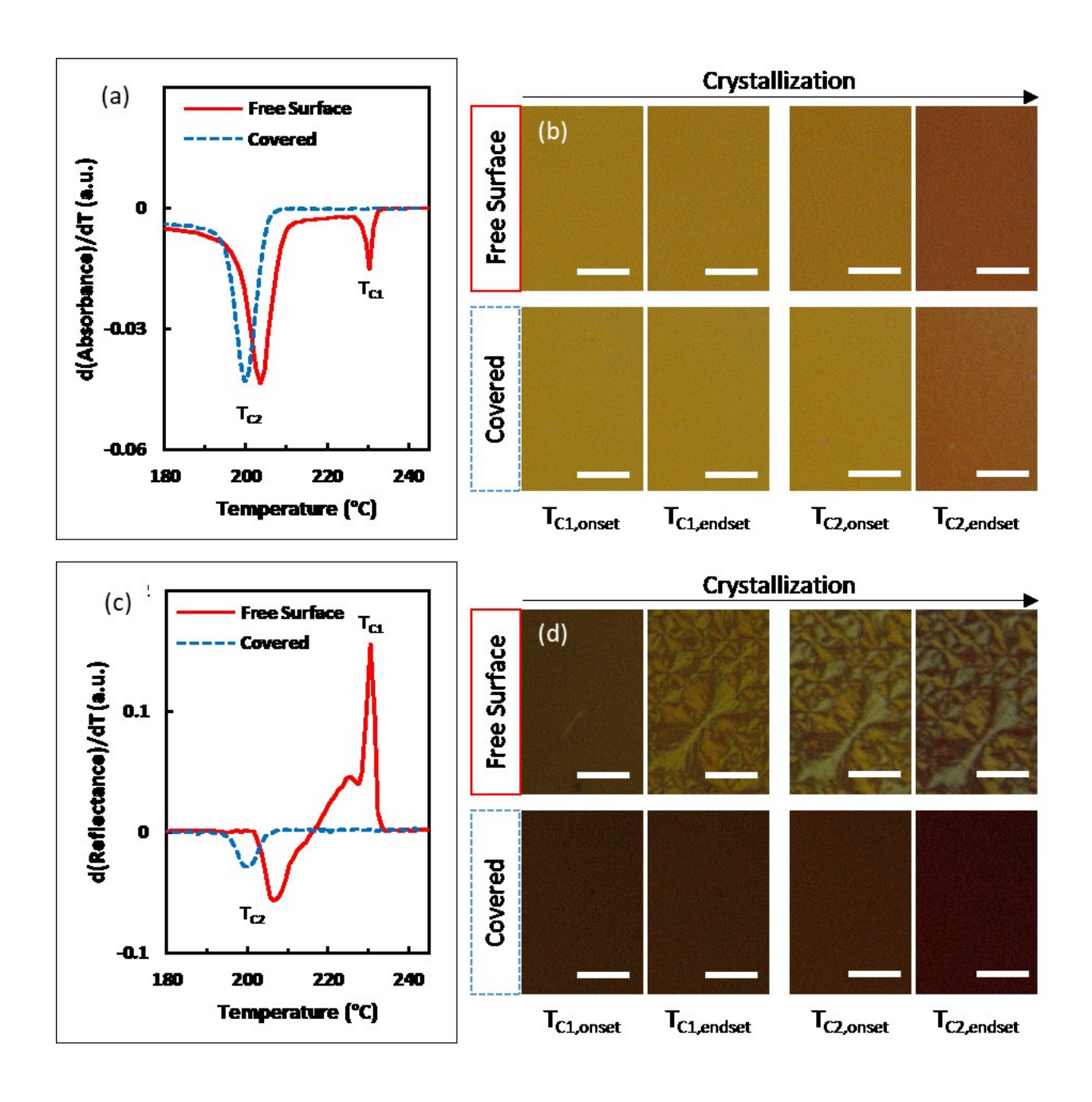


Figure 4: (a) Absorbance derivative, (b) transmission micrographs, (c) polarized reflectance derivative, and (d) polarized reflection micrographs during crystallization of 250 nm P3HT films with either a free surface or a top cover glass. Scalebar is 30 μ m.

It is interesting to note that the free surface film exhibits a small, non-zero derivative between T_{C1} and T_{C2} absorbance derivative peaks—indicating that a slight amount of crystallization occurs

in that temperature range—while the covered film does not exhibit any change in absorbance until T_{C2} crystallization starts (Figure 4a). Therefore, the small absorbance increase between peaks is related to the free surface layer crystallites that form at T_{C1} and may arise from secondary crystallization within the surface layer or from a small amount of downward growth into the underlayer.

3.3 Free-surface layer thickness

The crystallization behavior of films with thicknesses h = 10-250 nm was examined with insitu absorbance measurements. Interestingly, absorbance derivative curves show that the area of the T_{C1} peak becomes larger with increasing thickness for $h \le 20$ nm but is nearly fixed for $h \ge 40$ nm (Figure 5a, b). The invariance of the T_{C1} area for 40-250 nm thin films implies that the amount of surface-induced crystals formed at high temperature is nearly constant regardless of h, suggesting that the surface layer that crystallizes at T_{C1} has a fixed thickness.

In contrast to the T_{C1} peak behavior, the area of the T_{C2} peak—which tracks bulk-like crystallization of the underlayer—clearly increases with thickness for h = 20-250 nm but is absent for h = 10 and 15 nm. Such behavior implies that the thickness of the underlayer increases with film thickness in the h = 20-250 nm range, and that there is essentially no underlayer in the two thinnest samples. In other words, for the h = 10 and 15 nm films, the free surface spherulitic layer formed at T_{C1} pervades the entire crystallizable thickness and thus precludes later bulk-like crystallization at T_{C2} . Given that the 20 nm film still has a T_{C2} peak, but the 15 nm film does not, the surface layer is inferred to have a thickness less than 20 nm.

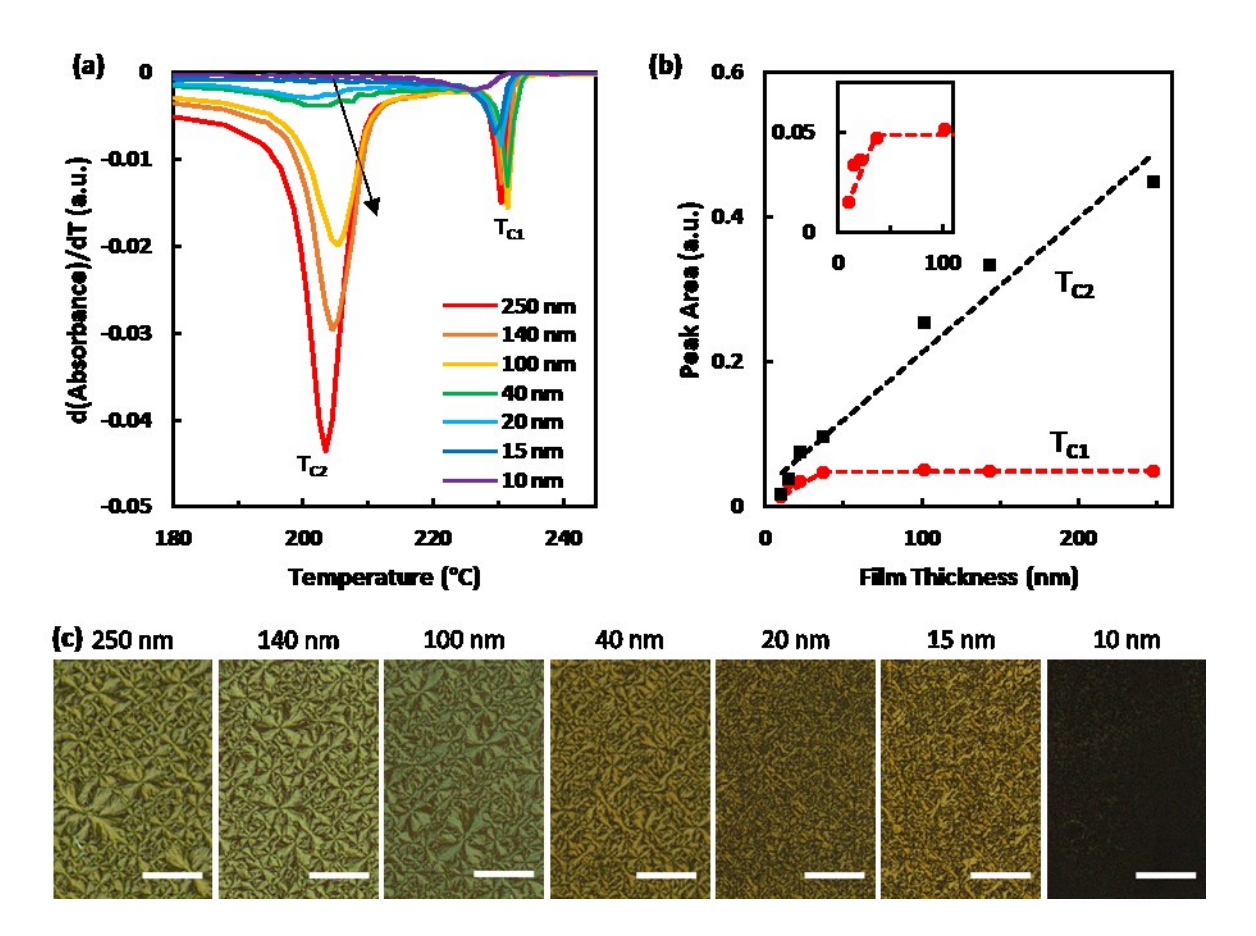


Figure 5: (a) Absorbance derivative during melt-crystallization of films with thickness h = 10-250 nm. Arrow indicates increasing h. (b) T_{C1} (circles) and T_{C2} (squares) peak areas vs. h. Inset shows close-up of T_{C1} peak area. Dashed lines are guide lines. (c) Ex-situ polarized reflection micrographs of films with various h. Scalebar is 50 μ m.

Large scale birefringent structures are evident at film thicknesses h=15-250 nm (Figure 5c). Films with $h \ge 100$ nm exhibit similar spherulitic structures with clear Maltese cross patterns, but films with h=15-40 nm show structures of progressively lower quality with decreasing thickness, which correlates with the decrease in T_{C1} area (Figure 5b). The temperature at which T_{C1} occurs is nearly constant for all films except for the thinnest (Figure 5a): the 10 nm film exhibits a ~4 °C

decrease in the T_{C1} peak temperature that correlates with the absence of large scale birefringent structures and may be indicative of substrate interactions or confinement effects.

3.4 In-situ GIWAXS

In-situ GIWAXS provides unique information about crystalline orientation, but the specific choice of incidence angle α_i determines whether scattering arises from the entire film or just from the top surface. Here, two different incidence angles were used— α_i = 0.08° and 0.14° (Figure 6)—which are below and above the critical angle $\alpha_c \sim 0.12^\circ$ of P3HT, respectively. For α_i = 0.08°, an evanescent wave occurs in the surface and probes only the top ~10 nm of the film. ⁵⁵ Because the spherulitic top layer of the films was estimated from absorbance to have a thickness of at most 20 nm, it is inferred that α_i = 0.08° primarily probes the top spherulitic layer. In contrast, at α_i = 0.14° the beam fully penetrates the sample so scattering arises from the entire thickness of the film. Two film thicknesses—40 and 250 nm—which exhibit very different amounts of T_{C2} crystallization (Figure 5b) were investigated.

In-situ GIWAXS of the 250 nm film shows clear differences between crystallization of the surface-only and of the entire thickness of the film (Figure 6a, compare α_i = 0.08° vs. 0.14°): the top ~10 nm develop only highly edge-on oriented crystallites which emerge at T_{C1} , while scattering from the entire film exhibits substantial isotropic crystallization at T_{C2} . During T_{C1} crystallization, the surface-only GIWAXS patterns (α_i = 0.08°) show the appearance of an extremely oriented (100) peak in the out-of-plane direction (white arrows in Figure 6a), which reveals that the free surface-induced spherulitic structures consist of highly oriented crystallites with alkyl chains stacked perpendicular to the free surface. At the end of T_{C1} crystallization, the lattice spacing in the alkyl chain direction is $d_{(100)}$ ~ 1.81 nm ($q_{(100)}$ ~ 0.348 Å-1) but decreases

sharply to $d_{(100)} \sim 1.74$ nm upon cooling to $T_{C2,onset}$. These lattice spacings are consistent with form I of P3HT—albeit slightly larger than the typically reported $d_{(100)} = 1.65$ nm, possibly due to thermal expansion. $^{20,\,27,\,56-58}$ Upon cooling through T_{C2} , the out-of-plane scattering at $\alpha_i = 0.08^\circ$ increases indicating that additional highly edge-on crystallization occurs within the top ~ 10 nm of the film. In contrast, scattering from the entire film ($\alpha_i = 0.14^\circ$) during T_{C2} shows that strong isotropic rings emerge in addition to increased out-of-plane scattering (most clearly observed in higher order diffraction peaks), i.e. T_{C2} crystallization of the bulk-like underlayer in the 250 nm film yields both edge-on and isotropic crystallites. Throughout the T_{C2} crystallization process, T_{C100} 0000 decreases very slightly to T_{C200} 1.72 nm.

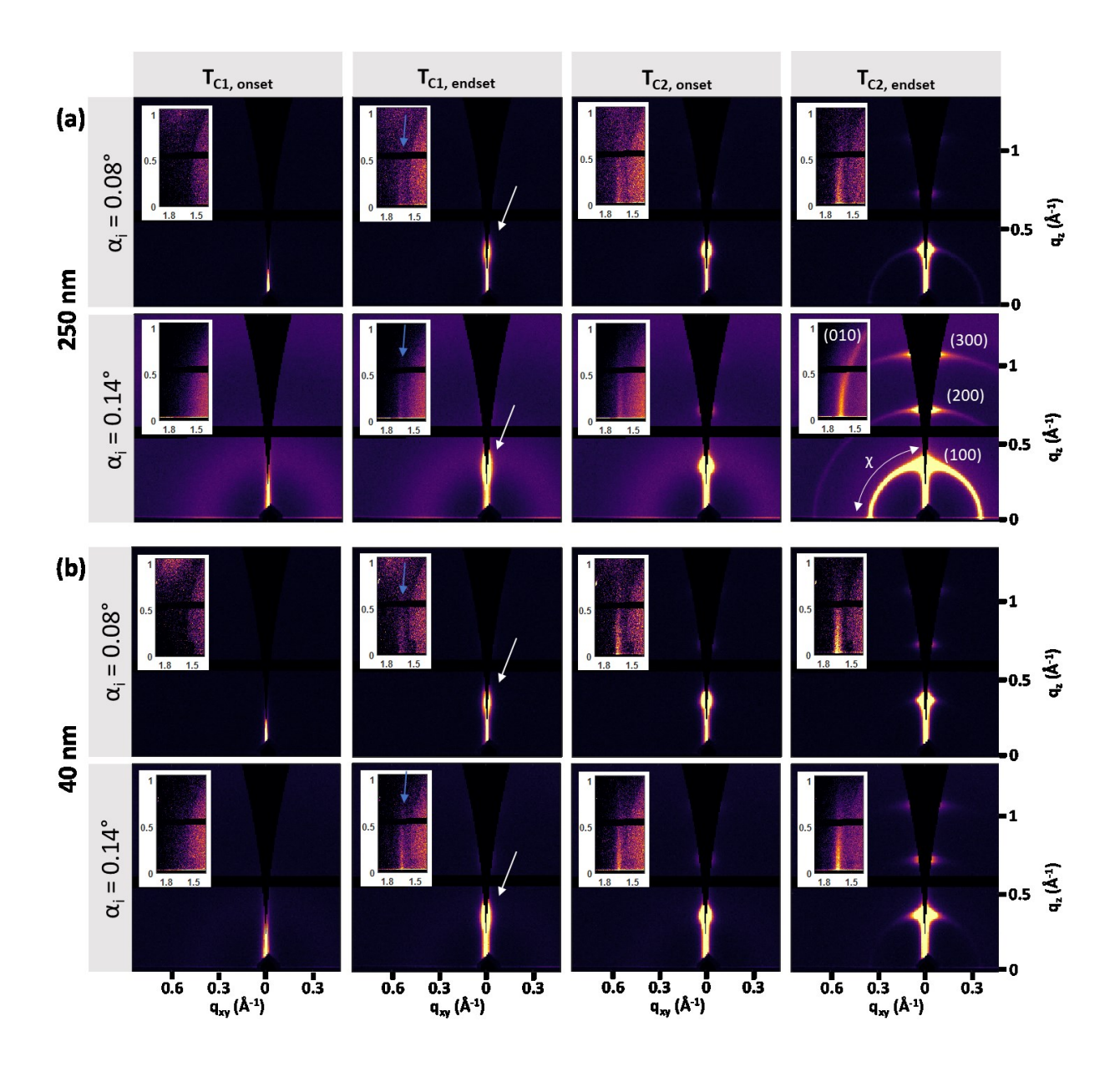


Figure 6: In-situ GIWAXS patterns at α_i = 0.08° and 0.14° during melt-crystallization of P3HT films with thickness of (a) 250 nm, (b) 40 nm. Insets show (010) in-plane scattering.

In stark contrast to the 250 nm film, the 40 nm film (Figure 6b) exhibits little to no isotropic scattering during crystallization at T_{C2} for α_i = 0.14°, indicating that the bulk-like underlayer of the 40 nm film crystallizes almost exclusively with edge-on orientation. The evolution of scattering at the top ~10 nm (α_i = 0.08°), however, closely resembles that of the top ~10 nm of the 250 nm

film, which indicates that crystallization and morphology of the surface layer is not affected by overall film thickness and is consistent with in-situ absorbance. Likewise, the evolution of $d_{(100)}$ in the 40 nm film is similar to that in the 250 nm film, and is also consistent with form I P3HT.

The emergence of out-of-plane (100) diffraction during T_{C1} is accompanied by the appearance of a highly oriented (010) in-plane Bragg rod at $d_{(010)} \sim 0.38$ nm $(q_{(010)} \sim 1.66 \text{ Å}^{-1})$ for both film thicknesses and incident angles, indicating that π - π stacking occurs during crystallization of the surface layer (blue arrow in Figure 6 insets, I vs. q plots shown in Figure S4 in Supplemental Data). The emergence of π - π stacking at T_{C1} is consistent with in-situ absorption and confirms that the free surface-induced crystallization involves the main chain of P3HT. Throughout T_{C2} crystallization, the highly oriented Bragg rod increases in intensity; in the case of the 250 nm film at $\alpha_i = 0.14^\circ$, additional (010) scattering emerges as an isotropic ring that overlaps with the Bragg rod. Interestingly, the paracrystallinity in the π - π stacking direction was calculated to be ~5.9, 6.8, and 7.9% at $T_{C1,endset}$, $T_{C2,onset}$, and $T_{C2,endset}$ respectively, which are similar values to those reported for fully solidified semicrystalline P3HT in literature (~7% for molecular weights beyond the chain folding limit)⁸ suggesting that the high temperature surface crystallites are as ordered (or slightly more so) in the π - π stacking direction than bulk P3HT crystallites.

The evolution of crystalline orientation can be quantified with pole figures where the sine-corrected intensity is proportional to crystallite volume at each azimuthal angle χ . In contrast to the 40 nm film, the overall orientation of the 250 nm film becomes dominated by isotropic crystallites as it is cooled through T_{C2} (Figure 7a, b). The edge-on/total crystallite fraction after melt-crystallization (ex-situ) was estimated for films with h = 15 - 250 nm, revealing that the edge-on fraction strongly decreases with increasing film thickness (Figure 7c). Given that the

surface layer is predominantly edge-on oriented (Figure 6), it is inferred that increased isotropic contribution with increased film thickness arises exclusively from the bulk-like underlayer. However, the underlayer is not exclusively isotropic: it contains mostly edge-on crystallites in thinner films and both edge-on and isotropic crystallites in thicker films. For example, if the underlayer were exclusively isotropic, the 40 nm film would be expected to have a maximum of \sim 50% edge-on crystallites (since the thickness of the edge-on surface layer is at most 20 nm); instead, it shows an edge-on fraction of 90% indicating the presence of substantial edge-on crystallites in the underlayer. Likewise, the 150 nm film would be expected to have a maximum of \sim 13% edge-on orientation, instead of the 58% observed. Note that the edge-on fraction in Figure 7c is slightly underestimated due to the missing wedge out of plane (χ < 2°).

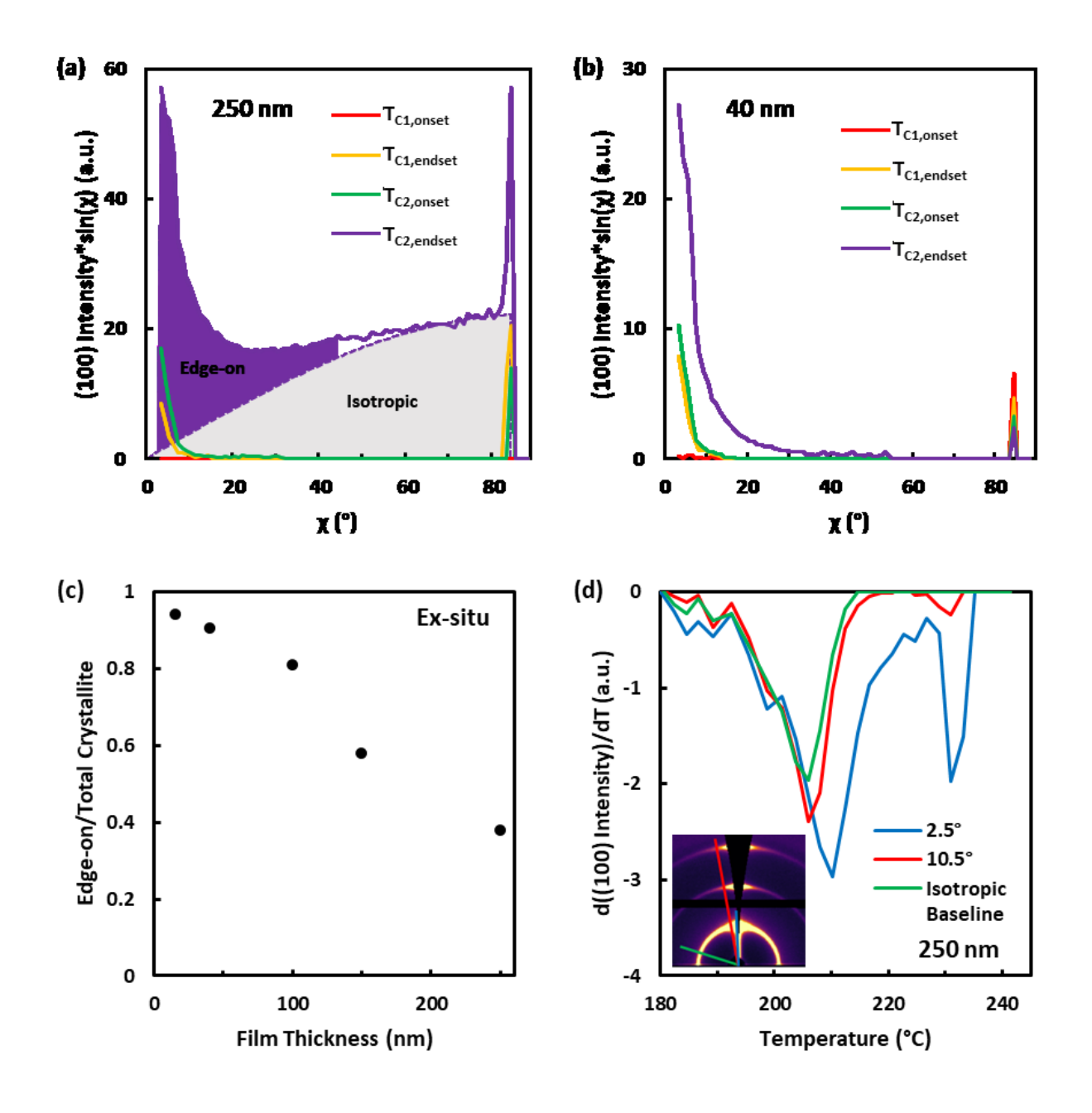


Figure 7. GIWAXS (100) partial pole figures at α_i = 0.14° during melt-crystallization of (a) 250 nm and (b) 40 nm thick films. Shaded areas represent the integrated edge-on and isotropic scattering. (c) Ex-situ edge-on crystallite fraction vs. film thickness (α_i = 0.14°). (d) (100) peak

intensity derivative (α_i = 0.14°) at χ = 2.5°, 10.5°, and the isotropic baseline during melt-crystallization of 250 nm film. Inset indicates χ = 2.5°, 10.5°, and 72.5°.

The results above are consistent with nucleation of edge-on crystallites on the underside of the surface crystallized layer at T_{C2}, which then grow downwards. During their growth into the bulk underlayer, those edge-on crystallites may pervade the underlayer in thinner films (resulting in edge-on only underlayers) or they become increasingly misoriented and eventually isotropic if the film is thick enough (resulting in both edge-on and isotropic contributions); it is also possible that independent nucleation events in the underlayer contribute partially or fully to T_{C2} isotropic growth. The evolution of the (100) peak intensity derivative at various χ for the 250 nm film (Figure 7d, I vs. q plots shown in Figure S5 in Supplemental Data) is consistent with an underlayer solidification process that begins with highly oriented growth but progressively diverges in orientation: the T_{C2} peak emerges earlier for highly oriented edge-on crystallites ($\chi = 2.5^{\circ}$) than for those slightly misoriented ($\chi = 10.5^{\circ}$). Conversely, growth of isotropic crystallites ($\chi = 72.5^{\circ}$) is concomitant with $\chi = 10.5^{\circ}$ crystallites rather than being further delayed, which suggests substantial independent nucleation of isotropic crystallites in the underlayer for h = 250 nm. The comparison of covered vs. uncovered in-situ UV-vis supports that crystallization of the underlayer is likely induced by surface crystallites. If the surface crystallized layer nucleates the edge-on crystallites (which appear before misoriented crystallites), then T_{C2} would be expected to decrease upon removing the free surface. Indeed, T_{C2} of the covered film is ~5 °C lower than that of the free surface film (Figure 4a).

The evolution of edge-on crystallite orientation during T_{C2} crystallization is also consistent with the growth of misoriented edge-on crystals in the bulk-like underlayer. To isolate the degree of orientation of edge-on crystallites, the isotropic contribution in the pole figures (Figure 7a, b) was subtracted before calculating the azimuthal (along χ) full width half max (FWHM). It was found that the overall orientation of edge-on crystallites does decrease during solidification of the bulk-like underlayer: the azimuthal FWHM of edge-on crystallites is ~10° at $T_{C1,endset}$ and ~11° at $T_{C2,onset}$ for both film thicknesses, but significantly increases throughout T_{C2} crystallization to 14° and 17° for h=40 and 250 nm respectively (Figure S3 in Supplemental Data). The greater decrease in edge-on orientation in the 250 nm film may arise from its thicker underlayer, where edge-on crystals nucleated on the top layer can grow further and misorient to a greater extent; it is also possible that solidification of a thicker underlayer generates a rougher surface and contributes to an apparent decrease of orientation.

4 Discussion

For the first time, a distinct free surface-induced melt-crystallization process which is confined within the top 20 nm layer of the film, crystallizes ~25 °C higher than the rest of the film, and exhibits extremely high edge-on orientation and large-scale birefringent spherulitic morphology has been directly observed in P3HT thin films. A direct comparison is made between P3HT thin films with and without a free surface that unequivocally ascribes the high temperature crystallization event and large-scale spherulitic morphology as free surface effects. Because surface-induced melt-crystallization is confined to a very thin layer at the surface, the overall final

morphology of films is highly dependent on thickness. Indeed, films with thickness $h \le 40$ nm are dominated by the free surface-induced morphology and overall display a high degree of edge-on orientation, while thicker films (h > 40 nm) consist of a highly edge-on oriented surface layer that is at most 20 nm thick, and a bulk-like underlayer with edge-on and isotropic contribution. Consequently, melt-crystallization provides an opportunity to tailor morphology and orientation across vertical strata of thin films for specific applications. The implications for design and processing of active layers in electronic devices—where electronically-relevant processes may occur near specific film interfaces or involve the entire thickness of the film—are evident.

A 2-step stratified melt-crystallization sequence during cooling of P3HT films is proposed in Figure 8. The schematic depicts two films with different thicknesses (both > 20 nm, i.e. an underlayer is present in both films). During T_{C1} crystallization, highly edge-on oriented spherulitic disc-like structures grow and impinge in the plane of the film confined at the free surface while the bulk-like underlayer remains molten. The thickness of the surface layer crystallized at T_{C1} is the same for both films regardless of overall film thickness. Upon cooling through T_{C2} , highly oriented edge-on crystallites nucleate on the underside of the surface layer, grow downwards into the bulk underlayer, and progressively diverge in orientation. If the film is thick enough, the growing edge-on crystallites may eventually diverge enough that isotropic orientation is attained, or isotropic crystallites may independently nucleate in the underlayer (Figure 8 bottom). In a thinner film, however, edge-on oriented crystallites can grow throughout the entire thickness before significant divergence or independent nucleation occurs, resulting in the absence of isotropic crystallites (Figure 8 top).

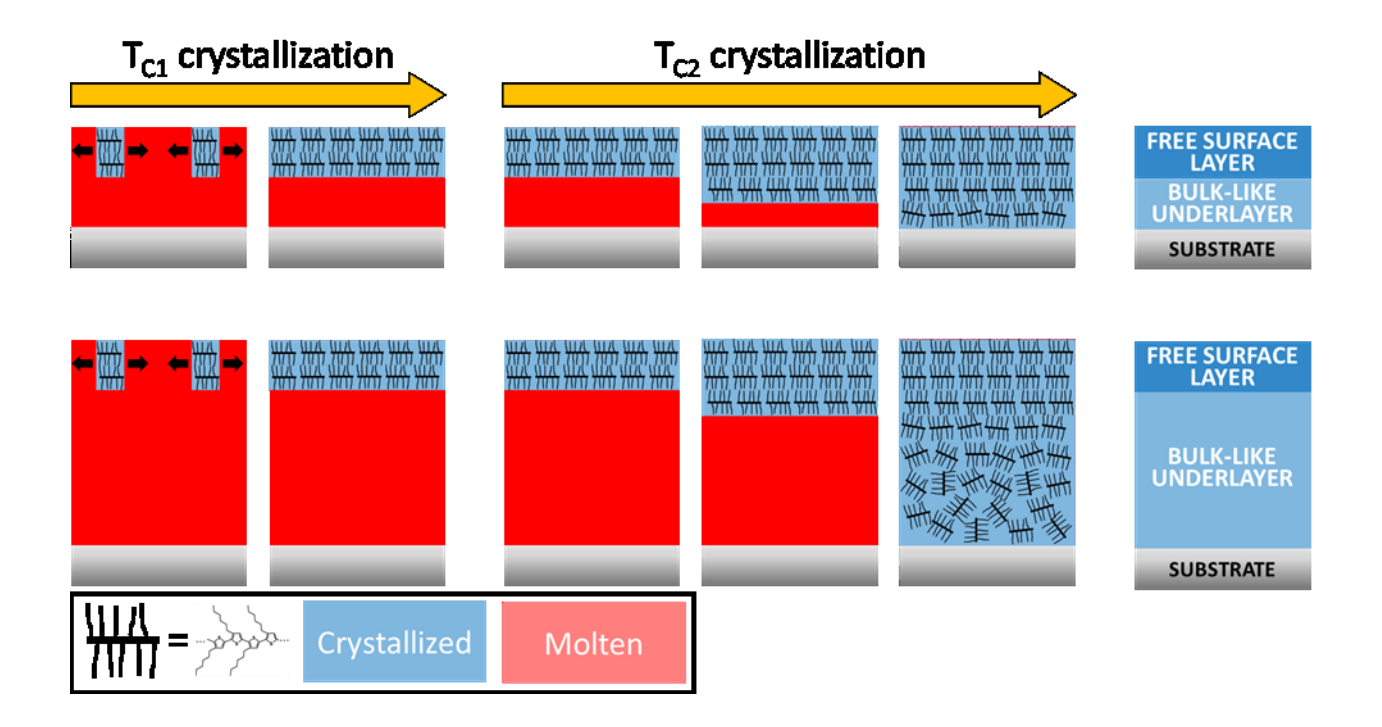


Figure 8: Proposed melt-crystallization sequence during cooling of P3HT films of different thicknesses.

The emergence of a crystallized free surface layer in P3HT at much higher temperature than bulk crystallization is attributed to a surface freezing phenomenon, where the alkyl side chains minimize the surface energy at the free surface by adopting a strong edge-on orientation and which results in substantially increased crystallization temperature. It is unclear, however, whether P3HT chains adopt the preferential edge-on orientation at the free surface prior to or during the crystallization process. Surface freezing effects have been proposed to explain a higher degree of edge-on orientation near the free surface of fully crystallized P3HT films (i.e. ex-situ),⁴³⁻⁴⁴ but the actual process of surface freezing during melt-crystallization of conjugated polymers has not been directly observed until now. Although surface freezing has been reported in poly(n-alkyl acrylates), it was only evident in crystallization of the alkyl side chains.^{40, 42} In contrast, the

surface freezing phenomenon detected here in P3HT involves main chain crystallization—i.e. π - π stacking and concurrent stacking of alkyl layers occur as shown by UV-vis absorbance and GIWAXS measurements (Figure 4a and Figure 7d). The 25 °C difference between surface and bulk-like crystallization observed here for P3HT is on the same order as that reported for poly(n-alkyl acrylate) (9-20 °C); in contrast, surface freezing in most non-polymeric materials results in at most a 3 °C increase of the surface transition temperature.⁵⁹

Although no evidence of pre-ordering of molecules (such as a liquid crystalline phase) prior to T_{C1} crystallization was detected in this study, it cannot be ruled out. Liquid crystalline phases have been reported in a few P3HT studies, $^{60-63}$ and modelling has predicted nematic-like alignment induced by an impenetrable interface. However, modelling has also predicted nematic-to-isotropic transitions that are very close to crystalline melting points in P3HT of high M_W (such as the material in this study), so whether a liquid-crystalline phase would be experimentally observable remains an open question. $^{65-66}$ In literature addressing surface freezing phenomena, both a smectic-like phase and side-chain crystallization have been reported on the film surface above bulk temperatures for poly(n-alkyl acrylate)s, 40 while other surface freezing studies only report crystalline phases. 35

Because the surface-induced layer morphology consists of large-scale birefringent spherulitic structures, P3HT provides the unique opportunity to directly observe the nucleation and growth behavior during crystallization of the surface layer. Typically, P3HT is thought to yield very high nucleating densities which preclude visualization of individual structures under optical

microscopy;^{11, 67} however, the top layer of the P3HT used in this work exhibits a nucleation areadensity on the order of $1000/\text{mm}^2$, resulting in large $10\text{-}50~\mu\text{m}$ spherulitic structures confined within the first 20 nm at the free surface. Because the spherulitic growth at T_{C1} consists of highly edge-on crystallites, the coherence length of the out-of-plane (100) reflection can provide a lower bound for the thickness of the surface frozen layer. Notably, the calculated out-of-plane (100) coherence length increases from ~3 nm for the first T_{C1} crystals to ~11 nm before bulk-like T_{C2} crystallization, which is commensurate with the <20 nm surface layer thickness inferred from optical experiments. Considering that P3HT has $d_{(100)} = 1.73$ nm, the surface layer may consist of 2-11 stacked alkyl layers. In contrast, the reported thickness of the surface frozen layer in poly(n-alkyl acrylates) is much thinner, with values of 0.79-1.5 nm that correspond to less than the length of one alkyl side chain.⁴²

5 Conclusion

In this work, a 2-step stratified melt-crystallization process is directly observed for the first time in P3HT films with thickness $h \ge 20$ nm: a thin layer (<20 nm) at the film free surface crystallizes at a temperature $T_{C1} \sim 25$ °C higher than the bulk crystallization temperature $T_{C,bulk}$, while the rest of the film (i.e. the underlayer) remains molten until crystallization near $T_{C,bulk}$. The high-temperature crystallization event is unequivocally attributed to the polymer/air interface: upon covering the film with glass, a free surface is not available and the T_{C1} crystallization process is absent. The high temperature crystallization process is nearly unchanged regardless of thickness for films $20 \le h \le 250$ nm, revealing a constant thickness for the free-surface crystallized layer. For films with h < 20 nm, the high temperature crystallization process is still present but

bulk-like underlayer crystallization is not observed, indicating that free surface effects dominate and providing an upper bound of 20 nm for the thickness of the surface-crystallized layer. For the thinnest film (h = 10 nm), surface-induced crystallization occurs at a slightly decreased temperature which may be indicative of substrate interactions or confinement effects.

The stratified melt-crystallization results in distinct morphologies at the surface layer and the underlayer. Free surface-induced crystallization at T_{C1} correlates with development of large, spherulitic structures at the air-polymer interface, which are absent in covered films. Furthermore, the surface layer only forms very highly oriented edge-on crystallites regardless of film thickness. In contrast, the underlayer morphology is highly dependent on the thickness of the underlayer: only edge-on oriented crystallites develop in thinner films ($h \le 40$ nm), while both edge-on and isotropic crystallites emerge in the underlayer of thicker films. Overall, our results underscore that melt-crystallization and free-surface effects can be used as a tool to manipulate morphology and orientation both at the free surface and across the thickness of thin films. Given that electronic device performance can be dictated by a few nm near an interface or by the entire thickness of the polymer film, melt-crystallization processing has the potential to optimize the properties of polymer active layers.

6 Acknowledgements

The authors gratefully acknowledge funding of this work by the National Science

Foundation under award DMR-1809888. X-ray scattering was performed at the Advanced

Photon Source, a U.S. Department of Energy (DOE) Office of Science user facility operated for

the DOE Office of Science by Argonne National Laboratory under Contract No. DE-ACO2-06CH11357. Profilometry was carried out at the NanoEngineering Research Core Facility (NERCF), which is partially funded by the Nebraska Research Initiative. The J.A. Woollam Foundation and Undergraduate Creative Activities and Research Experience (UCARE) program at University of Nebraska-Lincoln are also gratefully acknowledged for undergraduate research support.

<u>Supporting Information.</u> Bulk differential scanning calorimetry, example of GIWAXS analysis, representative I vs. q plots, azimuthal FWHM, thermal gradient experiments.

7 References

- 1. Burroughes, J. H.; Bradley, D. D. C.; Brown, A. R.; Marks, R. N.; Mackay, K.; Friend, R. H.; Burns, P. L.; Holmes, A. B., Light-emitting diodes based on conjugated polymers. *Nature* **1990**, *347* (6293), 539-541.
- 2. Yu, G.; Gao, J.; Hummelen, J. C.; Wudl, F.; Heeger, A. J., Polymer Photovoltaic Cells: Enhanced Efficiencies via a Network of Internal Donor-Acceptor Heterojunctions. *Science* **1995**, *270* (5243), 1789-1791.
- 3. Katz, H. E.; Bao, Z.; Gilat, S. L., Synthetic Chemistry for Ultrapure, Processable, and High-Mobility Organic Transistor Semiconductors. *Accounts of Chemical Research* **2001**, *34* (5), 359-369.
- 4. Bao, Z.; Dodabalapur, A.; Lovinger, A. J., Soluble and processable regioregular poly(3-hexylthiophene) for thin film field-effect transistor applications with high mobility. *Applied Physics Letters* **1996**, *69* (26), 4108-4110.
- 5. Li, G.; Shrotriya, V.; Huang, J.; Yao, Y.; Moriarty, T.; Emery, K.; Yang, Y., High-efficiency solution processable polymer photovoltaic cells by self-organization of polymer blends. *Nature Materials* **2005**, *4* (11), 864-868.

- 6. Chang, J.-F.; Sun, B.; Breiby, D. W.; Nielsen, M. M.; Sölling, T. I.; Giles, M.; McCulloch, I.; Sirringhaus, H., Enhanced mobility of poly (3-hexylthiophene) transistors by spin-coating from high-boiling-point solvents. *Chemistry of Materials* **2004**, *16* (23), 4772-4776.
- 7. Müller, C.; Zhigadlo, N. D.; Kumar, A.; Baklar, M. A.; Karpinski, J.; Smith, P.; Kreouzis, T.; Stingelin, N., Enhanced Charge-Carrier Mobility in High-Pressure-Crystallized Poly(3-hexylthiophene).

 Macromolecules 2011, 44 (6), 1221-1225.
- 8. Noriega, R.; Rivnay, J.; Vandewal, K.; Koch, F. P. V.; Stingelin, N.; Smith, P.; Toney, M. F.; Salleo, A., A general relationship between disorder, aggregation and charge transport in conjugated polymers.

 Nature Materials 2013, 12 (11), 1037-1043.
- 9. O'Connor, B.; Kline, R. J.; Conrad, B. R.; Richter, L. J.; Gundlach, D.; Toney, M. F.; DeLongchamp, D. M., Anisotropic Structure and Charge Transport in Highly Strain-Aligned Regioregular Poly(3-hexylthiophene). *Advanced Functional Materials* **2011**, *21* (19), 3697-3705.
- 10. Gu, K.; Snyder, C. R.; Onorato, J.; Luscombe, C. K.; Bosse, A. W.; Loo, Y.-L., Assessing the Huang–Brown Description of Tie Chains for Charge Transport in Conjugated Polymers. *ACS Macro Letters* **2018**, 7 (11), 1333-1338.
- 11. Crossland, E. J.; Rahimi, K.; Reiter, G.; Steiner, U.; Ludwigs, S., Systematic Control of Nucleation Density in Poly (3-Hexylthiophene) Thin Films. *Advanced Functional Materials* **2011**, *21* (3), 518-524.
- 12. Schulz, G. L.; Ludwigs, S., Controlled crystallization of conjugated polymer films from solution and solvent vapor for polymer electronics. *Advanced Functional Materials* **2017**, *27* (1), 1603083.
- 13. Wang, T.; Pearson, A. J.; Lidzey, D. G.; Jones, R. A., Evolution of structure, optoelectronic properties, and device performance of polythiophene: fullerene solar cells during thermal annealing. *Advanced Functional Materials* **2011**, *21* (8), 1383-1390.

- 14. Hosseinabad, R.; Kuebler, J.; Fernandez-Ballester, L., Combined role of regioregularity and molecular weight on melt-crystallization and self-nucleation of poly(3-hexylthiophene). *Polymer* **2022**, *259*, 125341.
- 15. Malik, S.; Nandi, A. K., Crystallization mechanism of regionegular poly(3-alkyl thiophene)s. *Journal of Polymer Science Part B: Polymer Physics* **2002**, *40* (18), 2073-2085.
- 16. Vakhshouri, K.; Gomez, E. D., Effect of Crystallization Kinetics on Microstructure and Charge Transport of Polythiophenes. *Macromolecular Rapid Communications* **2012**, *33* (24), 2133-2137.
- 17. Koch, F. P. V.; Rivnay, J.; Foster, S.; Müller, C.; Downing, J. M.; Buchaca-Domingo, E.; Westacott, P.; Yu, L.; Yuan, M.; Baklar, M.; Fei, Z.; Luscombe, C.; McLachlan, M. A.; Heeney, M.; Rumbles, G.; Silva, C.; Salleo, A.; Nelson, J.; Smith, P.; Stingelin, N., The impact of molecular weight on microstructure and charge transport in semicrystalline polymer semiconductors—poly(3-hexylthiophene), a model study. *Progress in Polymer Science* **2013**, *38* (12), 1978-1989.
- 18. Singh, C. R.; Gupta, G.; Lohwasser, R.; Engmann, S.; Balko, J.; Thelakkat, M.; Thurn-Albrecht, T.; Hoppe, H., Correlation of charge transport with structural order in highly ordered melt-crystallized poly(3-hexylthiophene) thin films. *Journal of Polymer Science Part B-Polymer Physics* **2013**, *51* (12), 943-951.
- 19. Duong, D. T.; Ho, V.; Shang, Z.; Mollinger, S.; Mannsfeld, S. C. B.; Dacuña, J.; Toney, M. F.; Segalman, R.; Salleo, A., Mechanism of Crystallization and Implications for Charge Transport in Poly(3-ethylhexylthiophene) Thin Films. *Advanced Functional Materials* **2014**, *24* (28), 4515-4521.
- 20. Brinkmann, M.; Rannou, P., Effect of Molecular Weight on the Structure and Morphology of Oriented Thin Films of Regioregular Poly(3-hexylthiophene) Grown by Directional Epitaxial Solidification.

 Advanced Functional Materials 2007, 17 (1), 101-108.
- 21. Alizadehaghdam, M.; Heck, B.; Siegenführ, S.; AlShetwi, Y. A.; Keheze, F. M.; Stäter, S.; Abbasi, F.; Reiter, G., Following isothermal and non-isothermal crystallization of poly (3-hexylthiophene) thin films by UV–vis spectroscopy. *Polymer* **2020**, *210*, 122959.

- 22. Verploegen, E.; Mondal, R.; Bettinger, C. J.; Sok, S.; Toney, M. F.; Bao, Z., Effects of thermal annealing upon the morphology of polymer–fullerene blends. *Advanced Functional Materials* **2010**, *20* (20), 3519-3529.
- 23. Michell, R. M.; Mueller, A. J., Confined crystallization of polymeric materials. *Progress in Polymer Science* **2016**, *54*, 183-213.
- 24. Balko, J.; Portale, G.; Lohwasser, R. H.; Thelakkat, M.; Thurn-Albrecht, T., Surface induced orientation and vertically layered morphology in thin films of poly(3-hexylthiophene) crystallized from the melt. *Journal of Materials Research* **2017**, *32* (10), 1957-1968.
- 25. Joseph Kline, R.; McGehee, M. D.; Toney, M. F., Highly oriented crystals at the buried interface in polythiophene thin-film transistors. *Nature Materials* **2006**, *5* (3), 222-228.
- 26. Dong, B. X.; Strzalka, J.; Jiang, Z.; Li, H.; Stein, G. E.; Green, P. F., Crystallization Mechanism and Charge Carrier Transport in MAPLE-Deposited Conjugated Polymer Thin Films. *ACS Applied Materials & Interfaces* **2017**, *9* (51), 44799-44810.
- 27. Joshi, S.; Pingel, P.; Grigorian, S.; Panzner, T.; Pietsch, U.; Neher, D.; Forster, M.; Scherf, U., Bimodal Temperature Behavior of Structure and Mobility in High Molecular Weight P3HT Thin Films. *Macromolecules* **2009**, *42* (13), 4651-4660.
- 28. Choi, D.; Jin, S.; Lee, Y.; Kim, S. H.; Chung, D. S.; Hong, K.; Yang, C.; Jung, J.; Kim, J. K.; Ree, M.; Park, C. E., Direct Observation of Interfacial Morphology in Poly(3-hexylthiophene) Transistors: Relationship between Grain Boundary and Field-Effect Mobility. *ACS Applied Materials & Interfaces* **2010**, *2* (1), 48-53.
- 29. Saito, M.; Koganezawa, T.; Osaka, I., Correlation between Distribution of Polymer Orientation and Cell Structure in Organic Photovoltaics. *ACS Applied Materials & Interfaces* **2018**, *10* (38), 32420-32425.
- 30. Zhan, L.; Li, S.; Xia, X.; Li, Y.; Lu, X.; Zuo, L.; Shi, M.; Chen, H., Layer-by-Layer Processed Ternary Organic Photovoltaics with Efficiency over 18%. *Advanced Materials* **2021**, *33* (12), 2007231.

- 31. Sullivan, P.; Jones, T. S.; Ferguson, A. J.; Heutz, S., Structural templating as a route to improved photovoltaic performance in copper phthalocyanine/fullerene (C60) heterojunctions. *Applied Physics Letters* **2007**, *91* (23), 233114.
- 32. Zhao, N.; Noh, Y. Y.; Chang, J. F.; Heeney, M.; McCulloch, I.; Sirringhaus, H., Polaron Localization at Interfaces in High-Mobility Microcrystalline Conjugated Polymers. *Advanced materials* **2009**, *21* (37), 3759-3763.
- 33. Coropceanu, V.; Cornil, J.; da Silva Filho, D. A.; Olivier, Y.; Silbey, R.; Brédas, J.-L., Charge transport in organic semiconductors. *Chemical reviews* **2007**, *107* (4), 926-952.
- 34. Jiang, L.; Dong, H.; Meng, Q.; Li, H.; He, M.; Wei, Z.; He, Y.; Hu, W., Millimeter-sized molecular monolayer two-dimensional crystals. *Advanced Materials* **2011**, *23* (18), 2059-2063.
- 35. Ocko, B.; Wu, X.; Sirota, E.; Sinha, S.; Gang, O.; Deutsch, M., Surface freezing in chain molecules: Normal alkanes. *Physical Review E* **1997**, *55* (3), 3164.
- 36. Ellison, C. J.; Torkelson, J. M., The distribution of glass-transition temperatures in nanoscopically confined glass formers. *Nature materials* **2003**, *2* (10), 695-700.
- 37. Zuo, B.; Xu, J.; Sun, S.; Liu, Y.; Yang, J.; Zhang, L.; Wang, X., Stepwise crystallization and the layered distribution in crystallization kinetics of ultra-thin poly (ethylene terephthalate) film. *The Journal of Chemical Physics* **2016**, *144* (23), 234902.
- 38. Xu, Q.; Zhu, N.; Fang, H.; Wang, X.; Priestley, R. D.; Zuo, B., Decoupling role of film thickness and interfacial effect on polymer thin film dynamics. *ACS Macro Letters* **2020**, *10* (1), 1-8.
- 39. Gautam, K. S.; Dhinojwala, A., Melting at Alkyl Side Chain Comb Polymer Interfaces. *Physical Review Letters* **2002**, *88* (14), 145501.
- 40. Gautam, K. S.; Kumar, S.; Wermeille, D.; Robinson, D.; Dhinojwala, A., Observation of novel liquid-crystalline phase above the bulk-melting temperature. *Physical review letters* **2003**, *90* (21), 215501.

- 41. Prasad, S.; Hanne, L.; Dhinojwala, A., Thermodynamic study of a novel surface ordered phase above the bulk melting temperature in alkyl side chain acrylate polymers. *Macromolecules* **2005**, *38* (7), 2541-2543.
- 42. Prasad, S.; Jiang, Z.; Sinha, S. K.; Dhinojwala, A., Partial crystallinity in alkyl side chain polymers dictates surface freezing. *Physical review letters* **2008**, *101* (6), 065505.
- 43. Dolynchuk, O.; Schmode, P.; Fischer, M.; Thelakkat, M.; Thurn-Albrecht, T., Elucidating the Effect of Interfacial Interactions on Crystal Orientations in Thin Films of Polythiophenes. *Macromolecules* **2021**, *54* (12), 5429-5439.
- 44. Balko, J.; Portale, G.; Lohwasser, R. H.; Thelakkat, M.; Thurn-Albrecht, T., Surface induced orientation and vertically layered morphology in thin films of poly (3-hexylthiophene) crystallized from the melt. *Journal of Materials Research* **2017**, *32* (10), 1957-1968.
- 45. Müller, C.; Andersson, L. M.; Peña-Rodríguez, O.; Garriga, M.; Inganäs, O.; Campoy-Quiles, M., Determination of Thermal Transition Depth Profiles in Polymer Semiconductor Films with Ellipsometry. *Macromolecules* **2013**, *46* (18), 7325-7331.
- 46. Gensch, M.; Schwartzkopf, M.; Brett, C. J.; Schaper, S. J.; Li, N.; Chen, W.; Liang, S.; Drewes, J.; Polonskyi, O.; Strunskus, T.; Faupel, F.; Müller-Buschbaum, P.; Roth, S. V., Correlating Optical Reflectance with the Topology of Aluminum Nanocluster Layers Growing on Partially Conjugated Diblock Copolymer Templates. *ACS Applied Materials & Interfaces* **2021**, *13* (47), 56663-56673.
- 47. Clark, J.; Chang, J.-F.; Spano, F. C.; Friend, R. H.; Silva, C., Determining exciton bandwidth and film microstructure in polythiophene films using linear absorption spectroscopy. *Applied Physics Letters* **2009**, *94* (16), 117.
- 48. Spano, F. C., Modeling disorder in polymer aggregates: The optical spectroscopy of regionegular poly (3-hexylthiophene) thin films. *The Journal of chemical physics* **2005**, *122* (23), 234701.

- 49. Jiang, Z.; Li, X.; Strzalka, J.; Sprung, M.; Sun, T.; Sandy, A. R.; Narayanan, S.; Lee, D. R.; Wang, J., The dedicated high-resolution grazing-incidence X-ray scattering beamline 8-ID-E at the Advanced Photon Source. *Journal of synchrotron radiation* **2012**, *19* (4), 627-636.
- 50. Jiang, Z., GIXSGUI: a MATLAB toolbox for grazing-incidence X-ray scattering data visualization and reduction, and indexing of buried three-dimensional periodic nanostructured films. *Journal of Applied Crystallography* **2015**, *48* (3), 917-926.
- 51. Smilgies, D.-M., Scherrer grain-size analysis adapted to grazing-incidence scattering with area detectors. Erratum. *Journal of Applied Crystallography* **2013**, *46* (1), 286-286.
- 52. Rivnay, J.; Noriega, R.; Kline, R. J.; Salleo, A.; Toney, M. F., Quantitative analysis of lattice disorder and crystallite size in organic semiconductor thin films. *Physical Review B* **2011**, *84* (4), 045203.
- Baker, J. L.; Jimison, L. H.; Mannsfeld, S.; Volkman, S.; Yin, S.; Subramanian, V.; Salleo, A.; Alivisatos, A. P.; Toney, M. F., Quantification of thin film crystallographic orientation using X-ray diffraction with an area detector. *Langmuir* **2010**, *26* (11), 9146-9151.
- 54. Page, K. A.; Kusoglu, A.; Stafford, C. M.; Kim, S.; Kline, R. J.; Weber, A. Z., Confinement-driven increase in ionomer thin-film modulus. *Nano letters* **2014**, *14* (5), 2299-2304.
- 55. Tolan, M., *X-Ray Scattering from Soft-Matter Thin Films*. 1 ed.; Springer Berlin, Heidelberg: 1999; p IX, 198.
- 56. Yuan, Y.; Zhang, J.; Sun, J.; Hu, J.; Zhang, T.; Duan, Y., Polymorphism and Structural Transition around 54 °C in Regioregular Poly(3-hexylthiophene) with High Crystallinity As Revealed by Infrared Spectroscopy. *Macromolecules* **2011**, *44* (23), 9341-9350.
- 57. Prosa, T. J.; Winokur, M. J.; McCullough, R. D., Evidence of a Novel Side Chain Structure in Regioregular Poly(3-alkylthiophenes). *Macromolecules* **1996**, *29* (10), 3654-3656.

- 58. Tashiro, K.; Ono, K.; Minagawa, Y.; Kobayashi, M.; Kawai, T.; Yoshino, K., Structure and thermochromic solid-state phase transition of poly (3-alkylthiophene). *Journal of Polymer Science Part B: Polymer Physics* **1991,** *29* (10), 1223-1233.
- 59. Wu, X.; Ocko, B.; Sirota, E.; Sinha, S.; Deutsch, M.; Cao, B.; Kim, M.-W., Surface tension measurements of surface freezing in liquid normal alkanes. *Science* **1993**, *261* (5124), 1018-1021.
- 60. Ho, V.; Boudouris, B. W.; Segalman, R. A., Tuning polythiophene crystallization through systematic side chain functionalization. *Macromolecules* **2010**, *43* (19), 7895-7899.
- 61. Hugger, S.; Thomann, R.; Heinzel, T.; Thurn-Albrecht, T., Semicrystalline morphology in thin films of poly (3-hexylthiophene). *Colloid and Polymer Science* **2004**, *282*, 932-938.
- 62. Park, M. S.; Aiyar, A.; Park, J. O.; Reichmanis, E.; Srinivasarao, M., Solvent evaporation induced liquid crystalline phase in poly (3-hexylthiophene). *Journal of the American Chemical Society* **2011,** *133* (19), 7244-7247.
- 63. Kleinhenz, N.; Rosu, C.; Chatterjee, S.; Chang, M.; Nayani, K.; Xue, Z.; Kim, E.; Middlebrooks, J.; Russo, P. S.; Park, J. O., Liquid crystalline poly (3-hexylthiophene) solutions revisited: Role of time-dependent self-assembly. *Chemistry of Materials* **2015**, *27* (7), 2687-2694.
- 64. Zhang, W.; Gomez, E. D.; Milner, S. T., Surface-induced chain alignment of semiflexible polymers. *Macromolecules* **2016**, *49* (3), 963-971.
- 65. Zhang, W.; Gomez, E. D.; Milner, S. T., Predicting nematic phases of semiflexible polymers. *Macromolecules* **2015**, *48* (5), 1454-1462.
- 66. Snyder, C. R.; Gomez, E. D., Phase behavior of poly (3-hexylthiophene-2, 5-diyl). *Journal of Polymer Science Part B: Polymer Physics* **2016**, *54* (13), 1202-1206.
- 67. Koch, F. P. V.; Heeney, M.; Smith, P., Thermal and structural characteristics of oligo (3-hexylthiophene) s (3HT) n, n= 4–36. *Journal of the American Chemical Society* **2013**, *135* (37), 13699-13709.